



Tunneling Splittings of the Protonated Water and Water Dimer

Tea Babić,¹  Mihael Eraković,²  Marko T. Cvitaš^{1,*}

¹ Faculty of Science, University of Zagreb, Department of Physics, Bijenička cesta 32, 10000, Zagreb, Croatia

² Ruđer Bošković Institute, Department of Physical Chemistry, Bijenička cesta 54, 10000, Zagreb, Croatia

* Corresponding author's e-mail address: mcvitas@phy.hr

RECEIVED: October 16, 2024 * REVISED: December 19, 2024 * ACCEPTED: December 23, 2024

THIS PAPER IS DEDICATED TO THE LATE PROFESSOR TOMISLAV CVITAŠ

Abstract: Tunneling splittings (TS) in the ground state (GS) and selected vibrationally excited states of hydronium and Zundel cation are determined using the recently-developed Jacobi fields instanton method in full dimensionality and results compared to the previous numerically exact calculations. It is found that the TSs for the states that have higher energy than the barrier height can still be accurate and follow the correct trends (relative to the GS TS) if the contribution of the transverse modes dominates the splitting. Rearrangements between adjacent minima in Zundel cation have been studied in terms of minimum-action paths. TSs due to monomer inversion and internal rotation have been converged for the GS and the excited lowest-frequency mode. Observation of the fine splittings in the lowest branch of its TS pattern due to bifurcations, which break bonds to the shared proton, is precluded by symmetry.

Keywords: instanton theory, tunneling splittings, vibrational spectra, WKB, semiclassical vibrational dynamics, quantum molecular dynamics, bound states, protonated water clusters.

INTRODUCTION

THE interest in studying protonated water clusters stems from their significance in aqueous chemistry. Solvated protons mediate charge transport in water^[1,2] and in biological environments.^[3] Hydronium and Zundel cations can be viewed as building blocks of larger clusters and of acidic water.^[4] Experimental measurements of the infrared spectra of protonated water clusters in gas phase reveal information about their interatomic interactions and vibrational dynamics.^[5–7] Coupled anharmonic potentials that govern motion in these clusters have multiple accessible minima separated by shallow barriers.^[4] It is relatively straightforward to calculate the vibrational structure of hydronium cation, but theoretical studies of larger clusters that aim to interpret and assign the spectra are challenging due to the high dimensionality and a large degree of ‘floppiness’ in these systems. New quantum dynamical methods are being developed for this purpose. Further development of the multi-configurational time-dependent Hartree (MCTDH) method^[8–11] was needed to describe the infrared spectrum of Zundel cation in a series

of studies.^[12,13] Vibrational configuration interaction (VCI) has been used to study hydronium,^[14] Zundel ion^[15] and larger clusters.^[16] More recently, vibrational tree tensor network methodology^[17] was applied to study bound states of Zundel cation.

In this work, we set ourselves a goal to calculate a particular feature in the infrared spectra, the energy shifts due to tunneling between equivalent minima in hydronium and Zundel cations. For this purpose, we use the approximate methodology based on the semiclassical instanton theory.^[18–22] Due to the highly anharmonic motion in these systems even in the ground state (GS), they present a challenge for approximate treatments. The comparison of our approximate results against the numerically exact therefore provides a valuable insight into how accurate the method is for the potential with such characteristics. In contrast to the exact treatments, our approach could easily be applied to estimate the tunneling splittings (TS) and tunneling rates in much larger clusters. In general, it can be applied to systems which allow one to evaluate the potential gradients at several thousand geometries.

Instanton theory for calculating tunneling splittings in molecules was first developed for the ground vibrational state in one dimension.^[23] Mil'nikov and Nakamura extended it to multidimensional systems^[18] and to the vibrationally excited states^[19] in an approach using Jacobi fields or, equivalently, modified WKB (Wentzel–Kramers–Brillouin) approximation. More recently, instanton theory in a ring-polymer form was developed^[20] for the GS, which can also treat multi-well systems.^[24] We generalized the original multi-dimensional instanton theory using Jacobi fields to multi-well systems for the ground^[21] and vibrationally excited states^[22] and showed that it is equivalent to the ring-polymer instanton theory in the GS. We also extended the method to treat inequivalent wells and inequivalent vibrational states in different wells.^[25] The above developments and the use of group theory made it possible to calculate the tunneling splitting patterns in a number of water clusters^[24,26–31] and thus to interpret the related experiments. Accurate calculations of TSs in these systems are scarce, however, the methodology was tested against the numerically exact results in malonaldehyde^[25] and vinyl radical.^[32] The present calculations are aimed to further test the method for a highly anharmonic potential, for systems with multiple minima and with low barriers for interconversion.

Such first-principles calculations of vibrational dynamics rest on the knowledge of the potential energy surface (PES) (and also the dipole moment surface). Methods for constructing these high-dimensionality PESs for the increased cluster sizes and with the increased accuracy have also been developing recently.^[33,34] In this work, we use the PES of Ref. 14 for hydronium and of Ref. 15 for Zundel cation. These PESs are fits of permutationally invariant polynomials to the CCSD(T) electronic energies using aug-cc-pVQZ and aug-cc-pVTZ basis sets, respectively. They were also used in the recent numerically exact bound state calculations^[9,11,14,35] which allows us to make a fair comparison below.

The paper is organized as follows. Section 2 reviews our semiclassical methodology for calculating TSs. Section 3a and 3b present the tunneling splittings in hydronium and Zundel cation, respectively. Conclusions follow in Section 4.

METHODOLOGY

In molecular systems with multiple equivalents, symmetry-related minima separated by high potential barriers, degenerate single-well vibrational states interact via tunneling. The tunneling interaction causes measurable energy shifts of the otherwise degenerate states, which we calculate below using the following methodology. Hamiltonian matrix is constructed using the single-well local vibrational states of all minima. Usually, one assumes

that different vibrational states of a single well are well separated in energy in comparison to the size of the tunneling interaction between them, which allows one to construct a separate matrix for each vibrational state. This so-called tunneling matrix (TM), with columns/rows labeled by the versions of minima, has the degenerate single well energies on diagonal, while off-diagonal elements account for the pairwise tunneling interaction between equivalent states of different minima. The diagonal state energies in the TM are usually set to zero and the eigenvalues of TM then give the relative energy shifts due to tunneling.

Tunneling interaction between degenerate single-well states of two different minima, i and j , can be evaluated using Herring formula^[36,37]

$$h_{ij} = \frac{1}{2} \int \phi^{(j)}(\mathbf{n} \nabla) \phi^{(i)} - \phi^{(i)}(\mathbf{n} \nabla) \phi^{(j)} d\Sigma \quad (1)$$

where $\phi^{(i/j)}$ are the single-well wavefunctions in wells i and j , Σ is the dividing surface with unit normal \mathbf{n} , placed inside the barrier which separates the two wells. [Eq. (1)] assumes the use of Cartesian mass-scaled coordinates and atomic units ($\hbar = 1$).

Single-well localized wavefunctions $\phi^{(i/j)}$ are obtained using modified WKB (M-WKB) approximation^[18,19,22,25] which results in an identical expression for the GS TS as the instanton theory. The wavefunction $\phi^{(i)}$ is constructed along the classical path on the inverted potential, $-V$, which starts off at minimum i with zero kinetic energy and leads to minimum j , the so-called instanton path. The trajectory is parametrized by the arc-length distance S from one minimum at $S = 0$ to the other minimum at $S = S_{\max}$. The path is thus a continuous sequence of molecular geometries $\mathbf{x}(S)$ in the f -dimensional mass-scaled coordinate space (f is the number of degrees of freedom). This unstable trajectory is found by minimizing the action

$$A = \int_0^{S_{\max}} p(S') dS' = \int_0^{S_{\max}} \sqrt{2V(S')} dS' \quad (2)$$

where $V(S)$ is potential at $\mathbf{x}(S)$, set to zero at minimum. $p(S)$ is the magnitude of the f -dimensional momentum

$$p(S) = \frac{d\mathbf{x}(S)}{d\tau} = \frac{d\mathbf{x}(S)}{dS} \frac{dS}{d\tau} = \mathbf{t}(S)p(S) \quad (3)$$

where τ is the elapsed time, \mathbf{t} is tangent to the path at S , $V(S)$ is potential at $\mathbf{x}(S)$ and $p(S) = \sqrt{2V(S)}$ from the conservation of energy. The wavefunction for the GS ($v = 0$) and the first excited state ($v = 1$) in the normal mode U_e with frequency ω_e at a point \mathbf{x} is,^[22]

$$\phi_i(\mathbf{x}) = \sqrt{\frac{\det \mathbf{A}_0}{\pi^f}} \sqrt{\frac{(2\omega_e)^v}{(2v-1)!!}} (F(S) + \mathbf{U}^\top(S) \Delta \mathbf{x})^v \times e^{-\frac{1}{2} \int_0^S \frac{\text{Tr}(\mathbf{A}(S') - \mathbf{A}_0)}{\rho(S')} dS'} e^{-\int_0^S \rho(S') dS' - \mathbf{p}^\top \Delta \mathbf{x} - \frac{1}{2} \Delta \mathbf{x}^\top \mathbf{A}(S) \Delta \mathbf{x}} \quad (4)$$

where $\Delta \mathbf{x} = \mathbf{x} - \mathbf{x}(S)$ is a displacement from the reference point on the path $\mathbf{x}(S)$ and we drop the indices ($i = j$) that label minima. The parameters $F(S)$, $\mathbf{U}(S)$ and $\mathbf{A}(S)$ along the path are determined by integrating the following equations^[22] along the path,

$$\rho(S) \frac{d}{dS} \mathbf{A} = \mathbf{H}(S) - \mathbf{A}^2(S) \quad (5)$$

$$\rho(S) \frac{d}{dS} \mathbf{U} = \omega_e \mathbf{U}(S) - \mathbf{A}(S) \mathbf{U}(S) \quad (6)$$

with initial conditions $\mathbf{U}(0) = \mathbf{U}_e$ and $\mathbf{A}(0) = \sqrt{\mathbf{H}(0)}$, where $\mathbf{H}(S)$ is Hessian of potential at $\mathbf{x}(S)$, and $F(S) = \mathbf{U}^\top(S) \mathbf{p}(S) / \omega_e$. At each reference point $\mathbf{x}(S)$ on the minimum action path (MAP), [Eq. (4)] represents a full-dimensional wavefunction in the whole coordinate space. The first two factors on the r.h.s. represent the normalization constant, tuned to match the harmonic-oscillator state at minimum. The next term is the prefactor for the first excited state, where $F(S)$ quantifies the shift of the nodal plane away from the MAP and $\mathbf{U}(S)$ traces the direction of the nodal plane along the MAP. In the 2nd line of [Eq. (4)], the first exponential factor describes the change of the amplitude due to the effect of the change of zero-point energies of local normal modes along the MAP, while the second factor describes the Gaussian shape of the wavefunction.

TM element h_{ij} is evaluated by inserting the wavefunctions $\phi^{(i)}$ and $\phi^{(j)}$ of the form given by [Eq. (4)] in Herring formula, [Eq. (1)]. Dividing surface Σ is set to be the plane orthogonal to the MAP at the maximum of the potential along the MAP, at $S = S_\Sigma$, and the wavefunctions, [Eq. (4)], on Σ are evaluated with respect to the closest reference point on the path, $\mathbf{x}(S_\Sigma)$. Then $(\mathbf{n} \cdot \nabla) = d/dS$ in [Eq. (1)] brings down a factor $\rho(S_\Sigma)$ in front of the product $\phi^{(i)} \phi^{(j)}$ in the integrand as the leading order contribution, while the linear term $\mathbf{p}^\top \Delta \mathbf{x}$ vanishes at \mathbf{x} on Σ . The remaining product of Gaussians can then be integrated over the $(f-1)$ -dimensional Σ analytically, one dimension at a time, in the diagonal representation of

$$\bar{\mathbf{A}} = \frac{\mathbf{A}^{(i)}(S_\Sigma) + \mathbf{A}^{(j)}(S_\Sigma)}{2} \Big|_\perp. \text{ The symbol } \perp \text{ means that the}$$

direction \mathbf{t} , which is an eigenvector of $\bar{\mathbf{A}}$ with zero eigenvalue, is excluded. For the excited states, mixed terms involving $F^{(i/j)} \mathbf{U}^{(j/i)}$ do not contribute as they are odd over the domain of integration. Pure F -terms give longitudinal (along the MAP) contribution, while U -terms give contribution of transverse modes (orthogonal to the MAP).

Numerical evaluation of the TM element h_{ij} starts by locating the MAP connecting minima i and j . An initial path is usually constructed by aligning the geometries of two minima at the least root-mean-square Euclidean distance between them in mass-scaled Cartesian coordinates. The path is then discretized into N equally-spaced molecular geometries by linear interpolation of their coordinates. The MAP is determined iteratively in a gradient-based search using string method.^[38,39] Convergence criterion is set to 10^{-6} a.u. for the largest magnitude of the perpendicular-to-path N f -dimensional action gradient at a discretization point along the string. The MAP is converged by progressively increasing the number of discretization points at subsequent optimizations. Up to $N = 400$ is used in this work. In the next step, cubic spline interpolants for molecular geometries $\mathbf{x}(S)$, potential $V(S)$ and Hessians $\mathbf{H}(S)$ are constructed, element by element, from their values at the discretization points. These are then used to solve [Eq. (5)] for $\mathbf{A}^{(i/j)}(S)$. Interpolants of $\mathbf{A}^{(i/j)}(S)$ are then constructed and used to solve [Eq. (6)] for each excited mode \mathbf{U}_e of interest. Due to $p(0) = 0$, there is a singularity at $S = 0$ in [Eqs. (5) and (6)] and the solution at a small $S = \varepsilon$ is obtained using a polynomial expansion^[22] of \mathbf{H} , \mathbf{A} and \mathbf{U} in S . We varied ε in the interval from $0.1 m_e^{1/2} a_0$ to $15 m_e^{1/2} a_0$ in our calculations below. TM elements are then calculated by evaluating Gaussian integrals in Herring formula. Dependence of TM elements on N and ε is used to assess their convergence. This is repeated for all pairs of minima and a TM is constructed for each vibrationally excited mode of interest. Eigenvalues of TM give the tunneling splitting spectrum and its eigenvectors determine the vibrational state symmetry, which can be used to work out the nuclear spin degeneracies and thus the allowed transitions and their intensity pattern.^[40]

Tunneling splittings obtained using this approach are identical^[18,21] to those obtained using the ring-polymer instanton theory for the GS.^[20] Computational effort is concentrated in the gradient evaluation for locating the MAP and the subsequent Hessian evaluation along the MAP. The theory works in full dimensionality and using Cartesian coordinates. It assumes that the electronic potential is quadratic in directions orthogonal to the MAP and that the rotational motion is decoupled and can be neglected.

RESULTS

Hydronium

Hydronium cation has a trigonal pyramidal minimum structure, analogous to the ammonia, and can undergo inversion via a tunneling process shown in Fig. 1. The barrier height of the double-well potential, also shown in Fig. 1, is 629 cm^{-1} . The MAP connecting two minima is

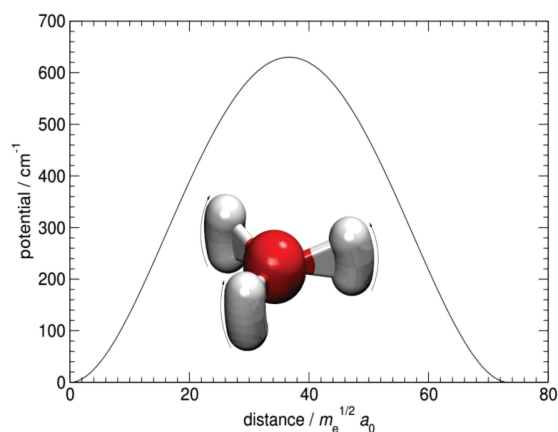


Figure 1. Potential along the minimum action path for the inversion of hydronium. Inset shows the sequential snapshots of molecular geometries along the minimum action path.

73.4 $m_e^{1/2}a_0$ long in mass-scaled coordinates, and has a symmetric potential profile with a barrier of 630 cm^{-1} , slightly higher than at the transition state. Corner-cutting effect in this system is minor.^[39] Minimum of action is at $3.68 \hbar$. Six normal modes of vibration, in order of increasing frequency, are the tunneling mode ν_1 in which the hydrogen plane moves along its normal at minimum, two degenerate asymmetric bend modes involving hydrogens $\nu_{2,3}$, symmetric stretch mode ν_4 , and two asymmetric OH stretches $\nu_{5,6}$.

Tunneling splittings obtained using M-WKB are given in Table 1 together with the numerically exact calculations of Ref. 14 on the same PES and the available experimental results.^[41–46] Harmonic frequencies of the normal modes are also given. TSs in the GS, which match our previous calculations in Ref. 39, and in the excited modes $\nu_{2,3}$ and $\nu_{5,6}$ are overestimated by up to 50 %. The comparative increase in the TS in mode $\nu_{2,3}$, relative to the GS TS, and the decrease in the excited mode $\nu_{5,6}$ are correctly predicted. The barrier height in the GS, corrected for the harmonic frequencies of perpendicular modes at transition state and the zero-point energy at minimum, is 270 cm^{-1} . The excited mode ν_1 is already an over-barrier vibrational state. The MAP tangent is a linear combination of modes ν_1 and ν_4 , so the two modes possess a large longitudinal component. This results in a large penetration of the wavefunction into the barrier region which violates the assumptions of M-WKB. The TS in the excited mode ν_1 is thus overestimated by a factor of 7, while the TS in mode ν_4 at 3608 cm^{-1} is not listed due to an unphysical result (above 10,000 cm^{-1}). The excited modes $\nu_{2,3}$ and $\nu_{5,6}$ lie significantly above the barrier at 3392 cm^{-1} and 3718 cm^{-1} . Given the approximations involved and the fact that TSs can vary over many orders of magnitude, the results for TSs in modes $\nu_{2,3}$ and $\nu_{5,6}$ are of

Table 1. Tunneling splittings in hydronium cation for the GS and the selected excited vibrational modes, in cm^{-1} . Experimental results, top to bottom, are taken from Refs. 41, 42, 43 and 44, respectively, and Refs. 45 and 46, for the last entry.

	ω_e	HCB	M-WKB	Expt.
GS	0	46	69	55.35
ν_1	871	354	2500	373.23
$\nu_{2,3}$	3392	57	87	67.92
ν_4	3608	37	–	46.16
$\nu_{5,6}$	3718	32	42	38.73

Table 2. Tunneling splittings in the fully deuterated hydronium cation for the GS and the selected excited vibrational modes, in cm^{-1} . Experimental results, top to bottom, are taken from Refs. 47, 47 and 48, respectively.

	ω_e	HCB	M-WKB	Expt.
GS	0	12	18	15.35
ν_1	659	174	830	191.39
$\nu_{2,3}$	1231	15	22	–
ν_4	2566	11	–	–
$\nu_{5,6}$	2733	7	10	9.94

expected accuracy for the instanton theories and of similar accuracy to the GS TS. We note that these modes have zero projection on the MAP along its full length, so they participate in internal energy redistribution along the MAP, but do not cause an exponentially increasing contribution to the wavefunction amplitude through [Eq. (6)]. We thus conclude that the TSs in the over-barrier states in the excited modes that have a significant longitudinal projection along the MAP cannot be adequately described by the M-WKB method.

We repeat the M-WKB calculations in the fully deuterated hydronium and list the results in Table 2 with the exact results of Ref. 14 and experiment.^[47,48] The MAP length is now increased to 96.6 $m_e^{1/2}a_0$, the zero-point-energy-corrected barrier height is 365 cm^{-1} and the action is $4.84 \hbar$. The GS TS is $3.8 \times$ reduced relative to H_3O^+ in both, the M-WKB and exact results. TSs in the GS and the excited modes $\nu_{2,3}$ and $\nu_{5,6}$ are overestimated by $\approx 50 \%$. For the same reason as above, the TS in the excited ν_1 mode is almost $5 \times$ too large, while the ν_4 mode again produces an unphysical result. These are again over-barrier states with large mode projections on the MAP.

In the partially deuterated species DH_2O^+ , normal modes ν_2 and ν_3 , as well as ν_5 and ν_6 are no longer degenerate. All the excited states ν_1 – ν_6 lie above the barrier

and only modes ν_2 and ν_6 have negligible projections on the MAP. TSs in the GS and the excited mode ν_2 are 50 cm^{-1} and 66 cm^{-1} . Exact results^[14] are again lower by a third at 33 cm^{-1} and 43 cm^{-1} . The excited mode ν_6 does not converge. We find that the unstable and large F -term in [Eq. (4)] is responsible. This suggests that the exponential increase of the negligibly small projection of the U vector on the MAP (at the level of numerical precision), as $\sim \exp(\omega_e \tau)$, results in an unphysical turning of the U vector towards the path. The excited ν_1 mode again overestimates the exact TS of 296 cm^{-1} to 1150 cm^{-1} , by a factor of 3.9. Similarly, in the doubly deuterated HD_2O^+ isotopologue, normal modes ν_3 and ν_5 have negligible MAP projections. Here, the TSs in the GS, the excited ν_3 and ν_5 modes are 33 cm^{-1} , 38 cm^{-1} and 30 cm^{-1} . Exact results^[14] are 22 cm^{-1} , 26 cm^{-1} and 7 cm^{-1} . The level of agreement is similar as above, apart from the TS in the excited ν_5 mode. Although the F -term is small in this case, the error likely comes from the exponential increase of errors in the transverse mode direction. In the excited mode ν_1 , the numerically exact TS is 236 cm^{-1} and the M-WKB TS again gives an unreliable overestimate at 1350 cm^{-1} (a factor of 5.7 discrepancy).

Zundel Cation

We next analyse the tunneling rearrangements in Zundel cation. These have first been characterized by Wales.^[49] We use here a more accurate electronic potential and analyse the rearrangements in terms of minimum-action paths, rather than the minimum-energy paths (MEPs), as was done in Ref. 49. The estimates of TM elements associated with each path are obtained using the M-WKB method,^[21,22] as described above.

The minimum energy structure of Zundel cation is shown in Fig. 2 labeled in its reference version. It belongs to the C_2 point group. The reference version is connected via degenerate tunneling rearrangements to other versions that are its permutational isomers. We consider those rearrangements that can be well represented by a single-barrier MAP connecting two 'adjacent' minima. The rearrangements can thus be labeled by the symmetry operation that converts the reference version at one end of the path to the minimum at the opposite end.

Molecular symmetry group of Zundel cation, if breaking of the covalent bonds on each water monomer is unfeasible, is G_{16} . This model assumes that the bonds to the shared hydrogen H5 are not allowed to break. Its elements include inversion, exchange of oxygens and exchange of hydrogens on each monomer, altogether $2 \times 2! \times (2!)^2 = 16$ elements. The character table is given in Table X in Ref. 49 and we adopt its names for irreducible representations. There are eight distinct minima which form a subgroup of G_{16} , since pairs of symmetry elements are related by a permutation (AB)(14)(23), which is

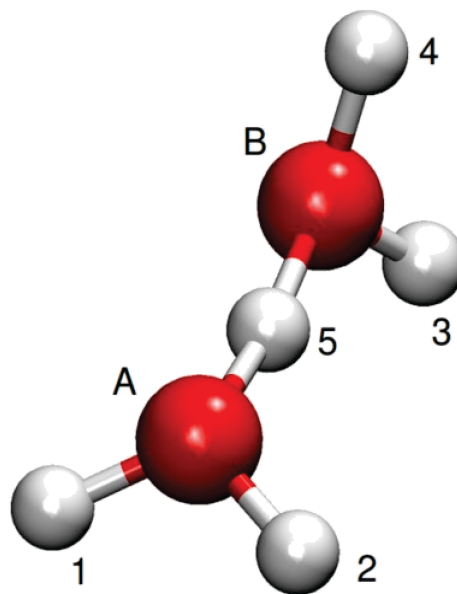


Figure 2. The minimum-energy geometry of Zundel cation labeled in its reference version.

equivalent to a C_2 rotation of the point group of the minimum structure.

Monomer inversion (mi) is the most facile motion. Its corresponding symmetry operation is $(12)^*$ for the inversion of monomer A, labeled by its oxygen atom, and $(34)^*$ for the inversion of monomer B. MAP connecting the minima related by monomer inversion is shown in Fig. 3 (a) (for the inversion of monomer B). Potential curve along the MAP, shown in Fig. 4, is symmetric and has a barrier of 167 cm^{-1} . It passes close to the C_s transition state, shown in Fig. 6 (a), at 164 cm^{-1} , which is a first-order saddle point. When we correct the barrier height for the zero-point motion of transverse modes at the transition state and the zero-point energy at minimum, the barrier is 95.5 cm^{-1} , which means that this is a tunneling process. The MAP length in mass-scaled coordinates is $81.42\text{ } m_e^{1/2} a_0$, 5.5 % shorter than the MEP, and results in the minimum action of $1.98\text{ } \hbar$.

Internal rotation of monomers A and B corresponds to the symmetry operation $(12)(34)^*$. Wales^[49] identified two mechanisms over which it proceeds and named them ir1 and ir2. Sequential snapshots of molecular geometries along the MAPs for ir1 and ir2 are shown in Fig. 3 (b) and (c), respectively. In ir1, monomers A and B rotate in positive and negative sense with respect to the vector AB and the MAP passes near a C_{2h} transition state, shown in Fig. 6 (b). Potential profile along the MAP in Fig. 4 is symmetric and passes through the first-order saddle point at 213 cm^{-1} . The barrier in the vibrational GS, corrected for the zero-point

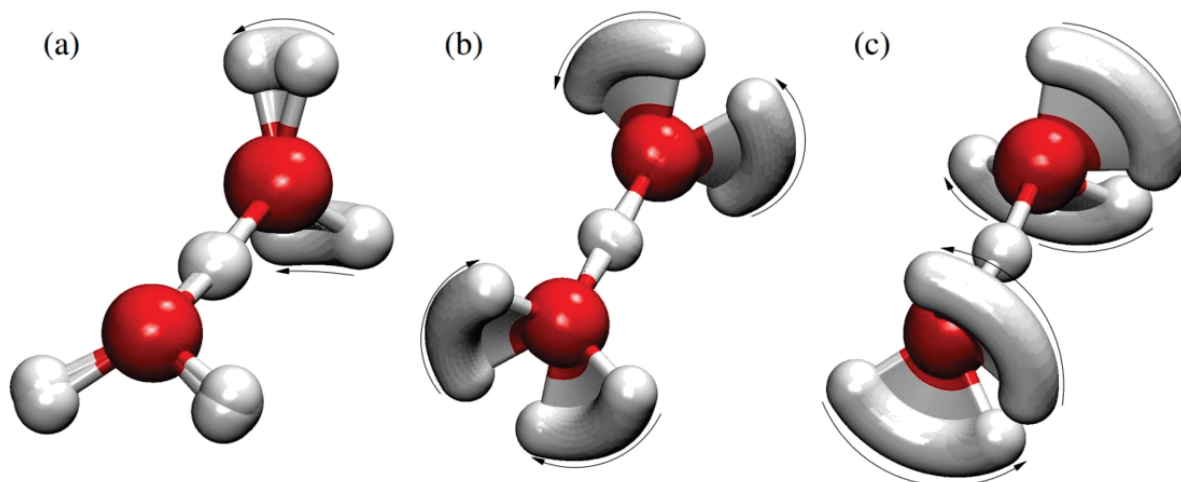


Figure 3. Minimum-action paths for monomer inversion (a) and internal rotations, (b) for ir1 and (c) for ir2 (see text), that are responsible for the formation of the tunneling splitting patterns in Zundel cation. Sequential snapshots of molecular geometries along the minimum-action paths are shown.

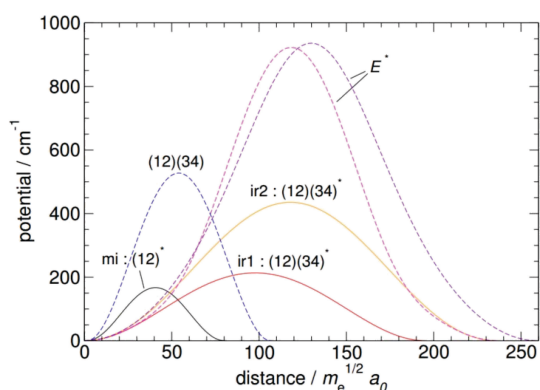


Figure 4. Potential along the minimum-action paths for monomer inversion, $(12)^*$, internal rotation, $(12)(34)^*$, via mechanisms ir1 and ir2, and for saddle points of action via paths to minima $(12)(34)$ and E^* in Zundel cation, shown in Figs. 3 and 5.

motion, is 155 cm^{-1} . The MAP length is $195.4\text{ m}_e^{1/2}a_0$ and the minimum of action is $5.60\hbar$. In ir2, monomers A and B rotate in the opposite senses to that in ir1 and the path passes over a C_{2v} transition state shown in Fig. 6 (c). Potential along the MAP is again symmetric, see Fig. 4, with the barrier along the MAP of 436 cm^{-1} , close to the first-order saddle point at 434 cm^{-1} . The barrier in the GS, corrected for the harmonic zero-point motion of transverse modes, is 266 cm^{-1} . The MAP length is $235.9\text{ m}_e^{1/2}a_0$ and the action is $9.31\hbar$. The MAPs for ir1 and ir2 practically coincide with MEPs, being only $\approx 0.2\%$ shorter. Both mechanisms contribute to the TM element for internal rotation, $(12)(34)^*$, additively.

The MAPs leading to the minima associated with the symmetry elements (12) and (34) decompose into the sequential two-step processes of $(12)(34)^* \times (34)^*$ and $(12)(34)^* \times (12)^*$, respectively, namely, into an internal rotation followed by a monomer inversion (or vice versa). The TM approach implicitly includes those contributions.

The search for the stationary-action path leading to the version obtained by applying the inversion operation, E^* , results in two possibilities. The path shown in Fig. 9 (b) is a second-order saddle point of action which passes near a D_{2h} transition state (not shown) with the barrier height of 923 cm^{-1} . The motion starts off with an internal rotation of type ir1 with the additional rotation of hydrogen atoms 1 and 4 about the AB axis towards the planar transition state and then proceeds symmetrically over the barrier resulting in a simultaneous inversion of monomers A and B. The length of the path is $236.9\text{ m}_e^{1/2}a_0$ resulting in the action of $11.42\hbar$. Another saddle point of action is shown in Fig. 9 (c). It initially follows the internal rotation ir2 with additional rotation of atoms 2 and 3 towards a D_{2h} transition state and symmetrically on the other side of the barrier at 936 cm^{-1} . The path length is $259.6\text{ m}_e^{1/2}a_0$ resulting in the action of $13.31\hbar$. Potential profiles along the two paths are shown in Fig. 4.

The transition state of both paths has three imaginary frequencies and their contributions to the TM element can therefore not be evaluated using the M-WKB approach. The rearrangement leading to the minimum E^* can also be achieved by a three-step process of internal rotation (ir1 or ir2) followed by two monomer inversions (in any order), $(12)(34)^* \times (12)^* \times (34)^*$, which have already been taken into account in the TM. The total action

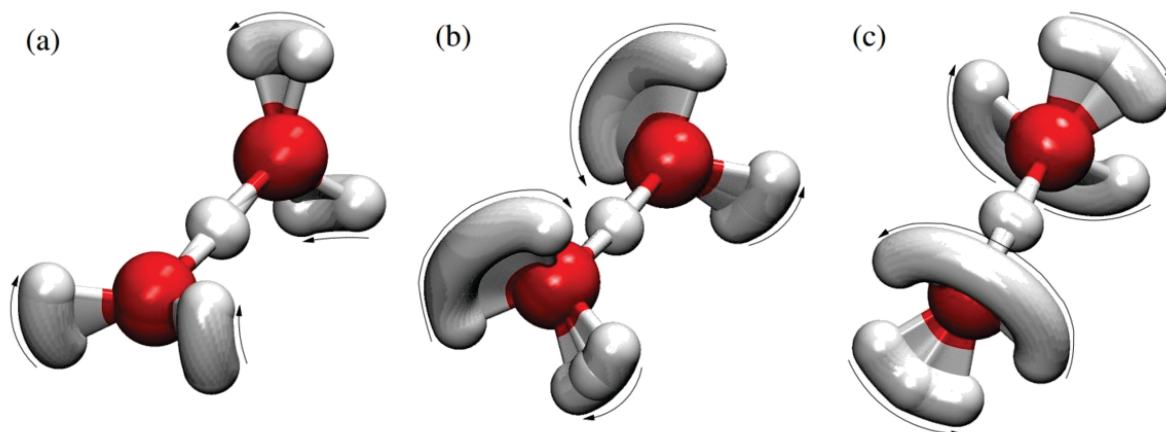


Figure 5. Saddle points of action for the paths leading to minima (12)(34), in (a), and E^* , in (b) and (c), in Zundel cation. Sequential snapshots of molecular geometries along the saddle-point action paths are shown.

integrals for these processes are $9.56 \hbar$ and $13.27 \hbar$, depending on whether the ir1 or ir2 route is taken. Based solely on the action contribution to the TM element, $\sim \exp(-A)$, the dominant contribution comes from the three-step ir1 path and a further contribution of $\approx 2.4 \%$ of its value comes from the three-step ir2 path. Two saddle-point processes potentially contribute $\approx 15.5 \%$ and 2.4% of a single 3-step process (with several of them contributing). Therefore, the neglect of these two paths probably contributes less than 10 % to the overall transition amplitude (see Fig. 8).

The optimized path leading to the minimum obtained by applying the symmetry element (12)(34) is a first-order saddle point of action. The motion involves a simultaneous inversion of monomers A and B, shown in Fig. 5 (a), which passes near a D_{2d} transition state (not shown), which is a second-order saddle point. Potential profile, shown in Fig. 4, is symmetric along the path with the barrier height of 527 cm^{-1} , the path length of $108.0 m_e^{1/2} a_0$ and the action of $4.75 \hbar$. Based on the exponential action contribution, the inclusion of this path could add a further 45 % to the transition amplitude connecting the corresponding minima in comparison to one of the two two-step processes (see Fig. 8) of sequential inversions of both monomers, $(12)^* \times (34)^*$, having the total action of $3.96 \hbar$. This process cannot be treated using M-WKB and has to be neglected. A more accurate treatment using, e.g., path-integral molecular dynamics,^[50,51] could involve sampling of the contributions around these saddle points of action as well.

If monomer inversions were the only feasible rearrangements, four versions of minima would be accessible: E , $(12)^*$, $(34)^*$ and $(12)(34)$, spanning the G_4 group. The group character table is given in Table IX of Ref. 49.

The 4×4 TM has two non-zero elements, h_{mi} , of equal size in each row and column. The TM is diagonalized to obtain the TS pattern. Its eigenvalues represent the vibrational state energies and the eigenvectors determine the symmetry of vibrational states. The monomer inversion tunneling splits the (single-well) degenerate GS of Zundel cation into a triplet^[49] with relative energies given by $2h_{mi}$, 0, and $-2h_{mi}$ for the A_1^+ , doubly-degenerate E^+ and B_2^+ states, respectively. The splitting pattern is schematically shown on the left half of Fig. 7.

We calculated the TM element h_{mi} in the GS and list the triplet splittings in the first two rows in Table 3 alongside the exact results of Ref. 9, obtained using MCTDH on the same PES. More recently, a larger number of vibrational states were calculated in Ref. 11, also using MCTDH and the same PES, and the splittings agree to within 4 % with the earlier MCTDH results. The two MCTDH numbers $\Delta(mi, 1)$ and $\Delta(mi, 2)$ refer to the lower, $E(E^+) - E(A^+)$, and upper, $E(B^+) - E(E^+)$, energy level separations of the triplet. Our TM model produces equally-spaced triplet and underestimates the splittings by $\approx 20\text{--}50 \%$. Inclusion of the TM element for the (12)(34) rearrangement (which cannot be obtained using M-WKB) would result in $\Delta(mi, 1) > \Delta(mi, 2)$. The more likely cause of the mismatch in the sizes of the two splittings is the presence of the excited vibrational states that are energetically in close proximity. The anharmonicity of the potential in directions perpendicular to the MAP also results in the deviations from the exact numbers, but the accuracy of the results is in line with the previous instanton calculations^[25,32,50] and with the results for hydronium cation above.

The motion in the lowest-frequency normal mode at $\nu_1 = 170 \text{ cm}^{-1}$ visually moves along the internal rotational motion (ir1 and ir2) of the two monomers. Wagging motion

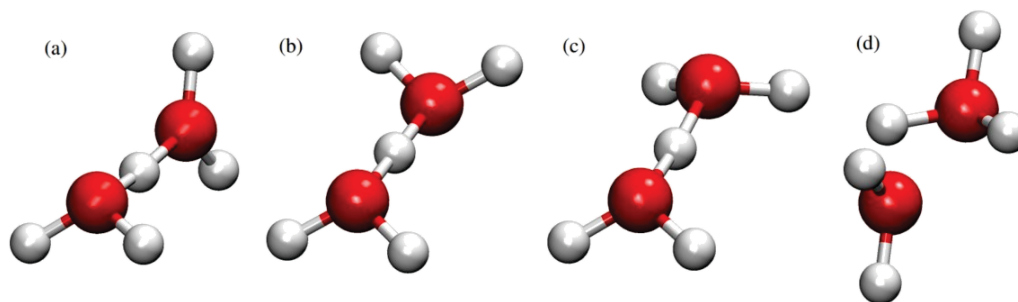


Figure 6. Transition state geometries of Zundel cation for monomer inversion $(34)^*$, in (a), internal rotations $(12)(34)^*$ via mechanism ir1, in (b), and ir2, in (c), and bifurcation mechanisms of monomer B, in (d).

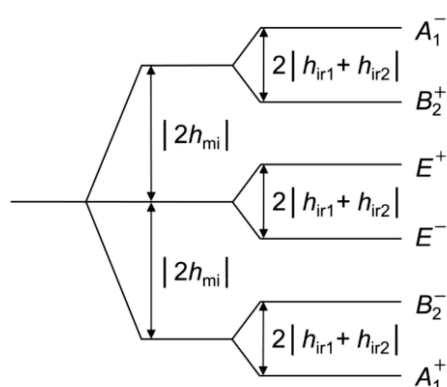


Figure 7. The diagram of tunneling splittings of a vibrational energy level in Zundel cation due to the monomer inversion (quantified by h_{mi}) and internal rotation (quantified by h_{ir1} and h_{ir2}).

of the monomers is the next lowest-frequency normal mode at $\nu_2 = 398 \text{ cm}^{-1}$. The excitation of those modes produces states that lie above the barrier height in energy. The M-WKB method has already been applied in this regime in hydronium cation with satisfactory results when the dominant contribution to the TM element comes from transverse modes (U -term). The longitudinal mode at minimum is the ν_1 mode, but the MAP shortly aligns along the ν_2 mode. We calculated the TM elements for the excited modes ν_1 . The dominant contribution to h_{mi} comes from the U -term (corresponding to the ν_2 mode). The corresponding splittings are also listed in Table 3 alongside the MCTDH results. The M-WKB splittings are reduced by 40 % relative to the GS TS, while the MCTDH results are largely unchanged. Again, the cause of the discrepancy, apart from the anharmonicity in transverse directions relative to the MAP, comes from the interaction with the other vibrationally excited states.

The TM element for the excited ν_2 mode is not listed ($h_{mi} \approx 200 \text{ cm}^{-1}$) since it is an over-barrier motion with a

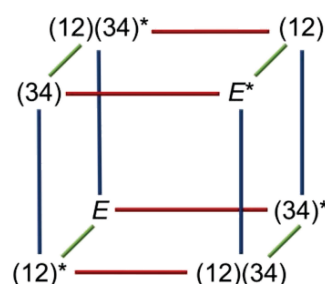


Figure 8. Graph of the connectivity between eight different minima of Zundel cation, related by permutation-inversion operations: by the mechanisms of inversion of monomers A and B, $(12)^*$ and $(34)^*$, and an internal rotation, $(12)(34)^*$. Green and red edges represent inversions of monomer A and B, respectively; blue edges represent internal monomer rotation.

large tangential (F -term) contribution, which likely results in a large overestimate. The main source of error here is probably the normalization to the harmonic-oscillator state and the large penetration of the single-well states into the barrier region. The off-diagonal interaction matrix elements between the GS- ν_1 , GS- ν_2 , ν_1 - ν_2 states, and also the

Table 3. Tunneling matrix (TM) elements of Zundel cation for rearrangement paths of molecular inversion (mi) and internal rotation (ir1 and ir2) in the vibrational ground state and the excited lowest-frequency vibrational mode in cm^{-1} .

Δ	GS		ν_1	
mi, 1	102.2	83	103.1	47
mi, 2	129.0		123.2	
ir, 1	0.9	1.9	15.3	59
ir, 2	1.5		21.4	
ir, 3	2.8		—	
	MCTDH	M-WKB	MCTDH	M-WKB

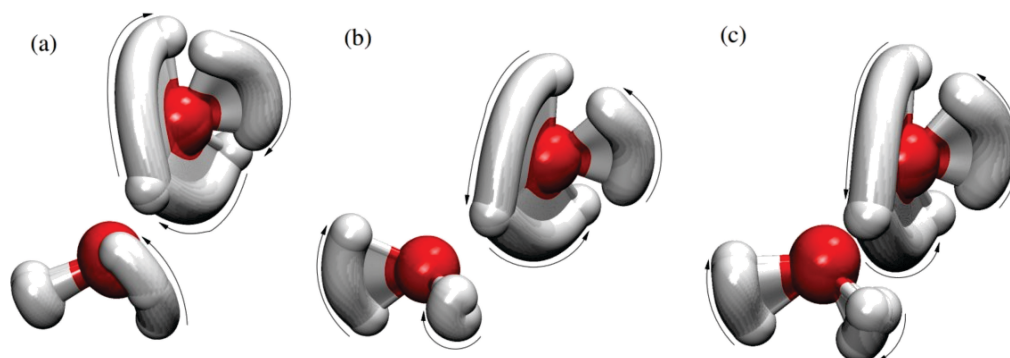


Figure 9. Minimum-action paths for three bifurcation mechanisms in Zundel cation: (a) for $(35)^*$, (b) for $(45)^*$ and (c) for (354) . Sequential snapshots of geometries along the minimum-action paths are shown.

interaction with the doubly-excited $2\nu_2$ state, are double-digit numbers in cm^{-1} . Those TM elements come at a degraded accuracy because they refer to the over-barrier motion, but their sizes suggest that they can significantly affect the splitting pattern. The utility of the combined M-WKB and TM approach is thus reduced when the sizes of the TM elements are of similar magnitude to the energy differences between the nearby states. In this case, the outcome is exacerbated by the fact that they lie above the barrier height in energy.

We have nevertheless calculated the splittings for the doubly-excited ν_1 mode with the dominant U -term (transverse) contribution and obtained $\Delta_{\text{mi},1/2} = 44 \text{ cm}^{-1}$. A further excitation of the ν_1 mode, therefore, does not significantly affect the splitting. This result is in agreement with the MCTDH calculation of Ref. 11, which gives $\Delta_{\text{mi},1/2} = 101.1 \text{ cm}^{-1}$ and $\Delta_{\text{mi},1/2} = 103.3 \text{ cm}^{-1}$, similar to the singly-excited ν_1 mode.

We now include internal rotation into the consideration, which brings access to eight versions of Zundel cation. The connectivity graph between minima connected by MAPs over the first-order saddle points is shown in Fig. 8. The dimension of the TM is therefore 8×8 . Each of its rows/columns has three non-zero elements, two are equal to h_{mi} (red and green line in Fig. 8) and one to $h_{\text{ir}} = h_{\text{ir}1} + h_{\text{ir}2}$ (blue line). Analytical expressions for the energy shifts due to tunneling can be obtained by constructing the symmetry-adapted state vectors of a particular irreducible representation of the G_{16} group and calculating the expectation values of the TM in symbolic form. The energy level diagram of tunneling states relative to the degenerate single-well state energy (without the presence of tunneling) is shown in Fig. 7. Internal rotation splits each branch of the triplet, that appears due to monomer inversion, into a doublet. All doublets have an equal width of $2|h_{\text{ir}}|$. The full width of the TS pattern is $|4h_{\text{mi}} + 2h_{\text{ir}}|$.

The comparison of the splittings for the GS and the excited ν_1 mode obtained using MCTDH^[9] and M-WKB is given in Table 3. $\Delta(\text{ir}, 1-3)$ refer to the ir doublets in A^+ , E^+ and B^+ (G_4 group labels) branches. The GS splittings due to internal rotation agree well with MCTDH. The MCTDH splittings for the excited ν_1 mode are increased by a factor of ≈ 15 , while we observe an increase by a factor of ≈ 30 . The excited ν_1 state lies close to the barrier top (about 15 cm^{-1} below in a harmonic approximation) and an overestimate for the longitudinal mode is not surprising. The contribution of ir1 path to h_{ir} amounts to 71 % and 86 % for the GS and the excited ν_1 state, respectively.

Our TM model predicts equal doublet widths in all triplet branches. MCTDH widths differ. The non-zero contribution of the (12)(34) rearrangement in Fig. 9 (a) does not change the doublet widths (it does, however, affect the triplet widths as commented above). The non-zero TM element for the E^+ path increases the doublet widths of the outer triplet branches, while it reduces the width of the mid branch in the GS. A non-zero element for (12) and (34) increases the width of the lower (A^+) doublet and reduces

Table 4. Tunneling matrix (TM) elements of Zundel cation for rearrangement paths of molecular inversion (mi) and internal rotation (ir1 and ir2) in the vibrational ground state and the excited lowest-frequency vibrational modes in cm^{-1} .

GS	$(\text{H}_2\text{O})_2\text{D}^+$		$(\text{D}_2\text{O})_2\text{H}^+$		$(\text{D}_2\text{O})_2\text{D}^+$	
mi, 1	99.0	104	51.9	31	49.6	42
mi, 2	127.5		83.0		84.4	
ir	–	1.8	–	0.16	0.06	0.15
ν_1						
mi, 1	101.0	61	65.4	17	66.5	23
mi, 2	123.4		88.3		89.4	
ir	–	54	–	7.1	–	6.5

the width of the upper doublet (B^+) in the GS. Nevertheless, the most significant cause of the unequal widths is likely the interaction with other single-well states that we excluded from our basis, as already discussed for the case of unequal triplet widths above.

We also reoptimized the MAPs and recalculated the TM elements for deuterated species, $(\text{H}_2\text{O})_2\text{D}^+$, $(\text{D}_2\text{O})_2\text{H}^+$ and $(\text{D}_2\text{O})_2\text{D}^+$ to study the isotope effect on the splittings. The results are summarised in Table 4. MCTDH results are taken from Ref. 35 and are listed left of M-WKB results. Deuteration in position 5 in Fig. 2 does not affect the MCTDH triplet splitting significantly, while it does result in an increase of 30–40 % using M-WKB. Agreement with the MCTDH results stays similar to that in $(\text{H}_2\text{O})_2\text{H}^+$. M-WKB predicts a slight decrease in the doublet widths of internal rotation upon D5 substitution. Using MCTDH, only the doublet width of the lowest two triplet branches of $(\text{D}_2\text{O})_2\text{D}^+$ was calculated at 0.06 cm^{-1} , close to, but still $2.5 \times$ smaller than 0.15 cm^{-1} obtained using M-WKB. Using M-WKB, we observe ≈ 30 – 40 times increase of doublet widths upon the excitation of ν_1 mode (MCTDH results for that are not available).

We next consider the bifurcation mechanisms that allows the breaking of O–H bonds to the shared proton. Wales^[49] determined the C_s transition state, shown in Fig. 6 (d), which is similar to the transition state for donor tunneling in water dimer and bifurcation mechanism in water trimer^[24] and pentamer.^[29] The transition state lies 3944 cm^{-1} above the minimum and 4550 cm^{-1} above the ground-state energy when corrected for the zero point motion of transverse modes of vibration. We found three bifurcation mechanisms that all pass near this first-order saddle point. Sequential snapshots of molecular geometries along the three MAPs are shown in Fig. 9.

The mechanism b1 shown in Fig. 9 (a) corresponds to the symmetry element $(35)^+$ and it involves the rotation of monomer B with the shared proton (the hydronium) around its C_3 axis, whereby H3 rotates into the place of H5 and H5 rotates towards where used to be H4, with a simultaneous inversion of monomer A (predominantly by the movement of H2). Potential along the MAP, shown in Fig. 10, is symmetric, the path length is $327.8\text{ }m_e^{1/2}a_0$. The rearrangement along the MEP breaks down into a two-step process of monomer inversion, followed by the bifurcation mechanism b2 discussed below. The MEP length is $402.2\text{ }m_e^{1/2}a_0$. The corner-cutting effect is thus significant here. The barrier along the MAP is 4069 cm^{-1} and the associated action $33.89\text{ }\hbar$. The equivalent mechanism, which involves the rotation of hydronium A with a simultaneous inversion of monomer B is associated with the symmetry element $(25)^+$ and the same TM element $h_{b1} = -1.2 \times 10^{-13}\text{ cm}^{-1}$ in the ground vibrational state.

The mechanism b2 shown in Fig. 9 (b) corresponds

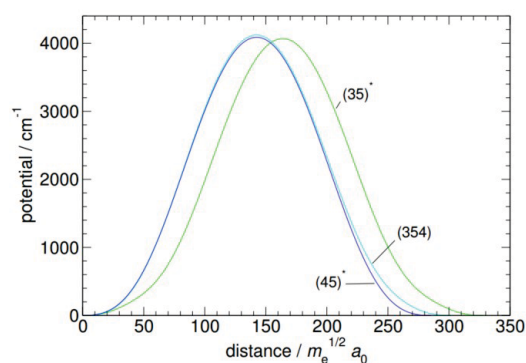


Figure 10. Potential along the minimum-action path for three different bifurcation mechanisms in Zundel cation: $(35)^+$, $(45)^+$ and (354) , shown in Fig. 9 (a), (b) and (c), respectively.

to the symmetry element $(45)^+$ and it involves the rotation of monomer B in the opposite sense to the b1 mechanism above, whereby H4 rotates into the place of H5 with a simultaneous inversion of monomer A. Potentials along the MAP, shown in Fig. 10, and MEP are symmetric, and the path lengths are $285.0\text{ }m_e^{1/2}a_0$. The barrier along the MAP is 4088 cm^{-1} and the associated action $31.47\text{ }\hbar$. The equivalent mechanism involving rotation of monomer A is associated with the symmetry element $(15)^+$. The corresponding GS TM element for both is $h_{b2} = -2.2 \times 10^{-13}\text{ cm}^{-1}$.

The mechanism b3 shown in Fig. 9 (c) corresponds to the symmetry element (354) . It involves rotation of hydronium B in the same sense as in $(45)^+$, without the inversion of monomer A. The similarity of initial motion of (354) and $(45)^+$ can be seen in potential profiles along MAP in Fig. 10. The MAP length of (354) is $301.6\text{ }m_e^{1/2}a_0$, while the MEP decomposes into a three-step process of monomer inversion, bifurcation b2 and another inversion, with a joint length of $488.5\text{ }m_e^{1/2}a_0$. The corner-cutting effect is substantial here. The barrier along the MAP is 4120 cm^{-1} , resulting in the action of $32.55\text{ }\hbar$. This is the only mechanism we found that has a slight asymmetry of the potential profile along the MAP, with the maximum at 47.2 % of the total path length (to the 'left' minimum associated with identity E). The inverse operation is (345) , while the corresponding symmetry elements involving the rotation of monomer B are (152) and (125) . All four mechanisms correspond to the identical TM element, $h_{b3} = -1.8 \times 10^{-13}\text{ cm}^{-1}$ in the GS.

All bifurcation TM elements h_{b1-3} are negligible. Past experiments^[31] in water clusters measure the tunneling splittings down to $\approx 10^{-5}\text{ cm}^{-1}$. The TM elements h_{b1-3} converge for the lowest six excited vibrational modes, ν_{1-6} . The excitation of ν_1 results in the enhancement of TM elements for b1–b3 by a factor 6.7, 2.2 and 4.0 relative to the GS TM element. The excitation of modes ν_2 and ν_3

results in double digit enhancements, while that of mode ν_5 and ν_6 in triple digit enhancements. The largest enhancements of more than $1000 \times$ are found for the excited mode ν_6 with TM elements $h_{b1-3} > 10^{-10} \text{ cm}^{-1}$, which still results in unmeasurable splittings. Nevertheless, we briefly analyse the splitting pattern in a hypothetical high precision experiment.

The inclusion of the bifurcation mechanisms b1–b3 generates a group of order 480, G_{480} . Oxygen atoms can be permuted (factor of 2!), five hydrogen atoms can take all positions in the molecule (factor of 5!) and inversion brings a factor of 2 in the element count. We constructed the character table of the group in Table 5 in Supplementary Information. The symmetry of the total internal wavefunction (the product of the rovibrational state and the nuclear spin state) must be either of $\Gamma^+ = A_3^+$ or $\Gamma^+ = A_3^-$ symmetry. In the ground rotational state, vibrational tunneling states have the following statistical weights: $\Gamma_{\text{vib}} = 2H_3^+ + 4G_3^+ + 6A_3^+$. The symmetry of the dipole operator is $\Gamma_{\text{dip}} = A_1^-$ and the allowed dipole transitions are of type $+$ \leftrightarrow $-$.

TM is of order 240, since pairs of minima related by the C_2 rotation of the point group C_2 are equivalent. Each row/column of the TM has 11 non-zero elements; two are identical and correspond to inversion of monomer A/B, one corresponds to the monomer rotation, while $8 = 2 + 2 + 4$ correspond to three nonequivalent bifurcation mechanisms discussed above. Experiments in water clusters often measure the bifurcation splittings of the lowest branch of the tunneling multiplet.^[31,52] The lowest sextet branch of A_1^+ symmetry in G_{16} , see Fig. 7, splits into six energy levels due to bifurcations having the following symmetries in G_{480} : A_1^+ , G_1^+ , H_1^+ , H_1^+ , G_1^+ , and H_3^+ . The energy separations are $a : a : 2a : a : a$, where $a = 1/2 (h_{b1} + h_{b2}) + h_{b3}$. Due to spin statistics, only the H_3^+ level is populated. Interestingly, it is actually the symmetry that precludes the observation of the splitting pattern due to bifurcations in Zundel cation. In a fully deuterated Zundel cation, all 6 levels are populated but the spacings are $\approx 10^{-18} \text{ cm}^{-1}$ in the GS.

In the sextet branch of B_2^- symmetry in G_{16} , see Fig. 7, five energy levels are populated (A_3^- , G_3^- , H_3^- , H_3^- , and G_3^-) and split as $a : a : 2a : a$. The E^- branch splits into two populated levels (G_3^- and H_3^-) separated by $3a$. Branches of symmetry E^+ and B_2^+ , in G_{16} , split as $3b$ and $b : 2b : b : b$, respectively, where $b = 1/2 (h_{b1} + h_{b2}) - h_{b3}$. The A_1^- branch populates only the H_3^- level.

CONCLUSIONS

We calculated the TSs of vibrational states in hydronium and Zundel cations, as well as some of their deuterated isotopologues, using M-WKB method. Both systems exhibit shallow minima. The rearrangements in the GS proceed via

tunneling, whereas vibrationally excited states in these systems lie above the barrier height in energy. We found that, in hydronium, TSs for the GS and the excited states that do not possess a significant longitudinal component relative to the MAP are $\approx 50 \%$ off from the numerically exact results. Increases and decreases of TSs relative to the GS TS upon the modal excitations, as well as trends upon deuteration, are correctly reproduced.

We studied the rearrangement pathways in Zundel cation by locating MAPs that connect adjacent minima in a similar fashion to the previous study in Ref. 49 using MEPs. The application of M-WKB to Zundel cation is complicated by the fact that the tunneling interaction matrix elements are of comparable size to the energy separation of different vibrational states and by the presence of more than two minima. With only the harmonic energies at our disposal, the energy shifts, due to presence of other vibrational states, cannot be accurately predicted. The splitting pattern in the TM approach consists of a triplet due to monomer inversion, whereby each of its branches is further split into a doublet by internal monomer rotation. Only the GS TS and the excited lowest frequency mode could be converged. The GS TSs are of similar quality to hydronium results, whereas the excited-state TSs are of lower quality due to the presence of the longitudinal component of the normal mode in an over-barrier state. Disappointingly, the trends of GS TSs upon deuteration are not all correctly reproduced. Nevertheless, M-WKB can still be applied to assess the sizes of the splittings at a negligible cost compared to the numerically exact approaches in this highly anharmonic and floppy molecule. We also determined the possible bifurcation mechanisms in Zundel cation, which break bonds to the shared proton, and worked out the corresponding TS pattern. Interestingly, the observation of the bifurcation splittings in the lowest branch of the sextet is precluded by symmetry.

A systematic improvement of the method in treating deep tunneling processes, such as bifurcations, is possible using perturbation theory,^[53] developed for the GS, or using higher-order WKB approaches.^[54] This would also allow us to make error estimates, but would bring an additional computational cost of having to evaluate the higher-order potential derivatives along the MAP. In order to improve the results for near- and over-barrier states, a modification of the ansatz is likely needed and will be investigated in future. In systems in which the size of the splitting is comparable to the energy differences between the vibrational states, as is the case in hydronium and Zundel cation, a mixed approach of calculating the interaction TM elements using M-WKB and local single-well vibrational energies using more accurate quantum-mechanical approaches, such as VCI, is possible,^[25] but the computational cost then becomes comparable to the exact quantum methods.

Acknowledgment. M. T. C. dedicates this work to the memory of his late father Tomislav Cvitaš. This work was fully supported by Croatian Science Foundation Grant No. IP-2020-02-9932.

Supplementary Information. Supporting information to the paper is attached to the electronic version of the article at: <https://doi.org/10.5562/cca4132>.

PDF files with attached documents are best viewed with Adobe Acrobat Reader which is free and can be downloaded from [Adobe's web site](https://www.adobe.com/acrobat/).

REFERENCES

- [1] O. F. Mohammed, D. Pines, J. Dreyer, E. Pines, E. T. J. Nibbering, *Science* **2005**, 310, 83–86.
<https://doi.org/10.1126/science.1117756>
- [2] A. Chandra, M. E. Tuckerman, D. Marx, *Phys. Rev. Lett.* **2007**, 99, 145901.
<https://doi.org/10.1103/PhysRevLett.99.145901>
- [3] G. Mathias, D. Marx, *Proc. Natl. Acad. Sci. U.S.A.* **2007**, 104, 6980–6985.
<https://doi.org/10.1073/pnas.0609229104>
- [4] D. Marx, M. E. Tuckerman, J. Hutter, M. Parrinello, *Nature* **1999**, 397, 601–604.
<https://doi.org/10.1038/17579>
- [5] J. M. Headrick, E. G. Diken, R. S. Walters, N. I. Hammer, R. A. Christie, J. Cui, E. M. Myshakin, M. A. Duncan, M. A. Johnson, K. D. Jordan, *Science* **2005**, 308, 1765–1769.
<https://doi.org/10.1126/science.1113094>
- [6] K. R. Asmis, N. L. Pivonka, G. Santambrogio, M. Brümmer, C. Kaposta, D. M. Neumark, L. Wöste, *Science* **2003**, 299, 1375–1377.
<https://doi.org/10.1126/science.1081634>
- [7] J. A. Fournier, C. T. Wolke, M. A. Johnson, T. T. Odbadrakh, K. D. Jordan, S. M. Kathmann, S. S. Xantheas, *J. Phys. Chem. A* **2015**, 119, 9425–9440.
<https://doi.org/10.1021/acs.jpca.5b04355>
- [8] O. Vendrell, F. Gatti, D. Lauvergnat, H.-D. Meyer, *J. Chem. Phys.* **2007**, 127, 184302.
<https://doi.org/10.1063/1.2787588>
- [9] O. Vendrell, M. Brill, F. Gatti, D. Lauvergnat, H.-D. Meyer, *J. Chem. Phys.* **2009**, 130, 234305.
<https://doi.org/10.1063/1.3152488>
- [10] M. Schröder, H.-D. Meyer, *J. Chem. Phys.* **2017**, 147, 064105. <https://doi.org/10.1063/1.4991851>
- [11] M. Schröder, *J. Chem. Phys.* **2020**, 152, 024108.
<https://doi.org/10.1063/1.5140085>
- [12] O. Vendrell, F. Gatti, H.-D. Meyer, *Angew. Chem.* **2007**, 46, 6918–6921.
<https://doi.org/10.1002/anie.200702201>
- [13] O. Vendrell, F. Gatti, H. Meyer, *Angew. Chem. Int. Ed.* **2009**, 48, 352–355.
<https://doi.org/10.1002/anie.200804646>
- [14] X. Huang, S. Carter, J. Bowman, *J. Chem. Phys.* **2003**, 118, 5431–5441.
<https://doi.org/10.1063/1.1555974>
- [15] X. Huang, B. J. Braams, J. M. Bowman, *J. Chem. Phys.* **2005**, 122, 044308.
<https://doi.org/10.1063/1.1834500>
- [16] Q. Yu, J. M. Bowman, *J. Chem. Phys.* **2017**, 146, 121102.
- [17] H. R. Larsson, M. Schröder, R. Beckmann, F. Brieuc, C. Schran, D. Marx, O. Vendrell, *Chem. Sci.* **2022**, 13, 11119–11125.
<https://doi.org/10.1039/D2SC03189B>
- [18] G. V. Mil'nikov, H. Nakamura, *J. Chem. Phys.* **2001**, 115, 6881–6897.
<https://doi.org/10.1063/1.1406532>
- [19] G. V. Mil'nikov, H. Nakamura, *J. Chem. Phys.* **2005**, 122, 124311.
- [20] J. O. Richardson, S. C. Althorpe, *J. Chem. Phys.* **2011**, 134, 054109. <https://doi.org/10.1063/1.3530589>
- [21] M. Eraković, C. L. Vaillant, M. T. Cvitaš, *J. Chem. Phys.* **2020**, 152, 084111.
<https://doi.org/10.1063/1.5145278>
- [22] M. Eraković, M. T. Cvitaš, *J. Chem. Phys.* **2020**, 153, 134106. <https://doi.org/10.1063/5.0024210>
- [23] A. I. Vainshtein, V. I. Zakharov, V. A. Novikov, M. A. Shifman, *Sov. Phys. Uspekhi* **1982**, 25, 195.
<https://doi.org/10.1070/PU1982v025n04ABEH004533>
- [24] J. O. Richardson, S. C. Althorpe and D. J. Wales, *J. Chem. Phys.* **2011**, 135, 124109.
<https://doi.org/10.1063/1.3640429>
- [25] M. Eraković, M. T. Cvitaš, *J. Chem. Theory Comput.* **2022**, 18, 2785–2802.
<https://doi.org/10.1021/acs.jctc.2c00124>
- [26] M. T. Cvitaš, J. O. Richardson, in *Molecular Spectroscopy and Quantum Dynamics*, ed. R. Marquardt and M. Quack, Elsevier **2020**, ch. 10.
- [27] M. Eraković, M. T. Cvitaš, *Phys. Chem. Chem. Phys.* **2021**, 23, 4240–4254.
<https://doi.org/10.1039/D0CP06135B>
- [28] M. Eraković, M. T. Cvitaš, *Phys. Chem. Chem. Phys.* **2024**, 26, 12965–12981.
<https://doi.org/10.1039/D4CP00013G>
- [29] M. T. Cvitaš, J. O. Richardson, *Phys. Chem. Chem. Phys.* **2019**, 22, 1035–1044.
<https://doi.org/10.1039/C9CP05561D>
- [30] J. O. Richardson, D. J. Wales, S. C. Althorpe, R. P. McLaughlin, M. R. Viant, O. Shih, R. J. Saykally, *J. Phys. Chem. A* **2013**, 117, 6960–6966.
<https://doi.org/10.1021/jp311306a>
- [31] J. O. Richardson, C. Pérez, S. Lobsiger, A. A. Reid, B. Temelso, G. C. Shields, Z. Kisiel, D. J. Wales, B. H. Pate, S. C. Althorpe, *Science* **2016**, 351, 1310–1313.
<https://doi.org/10.1126/science.aae0012>

- [32] M. Eraković, M. T. Cvitaš, *J. Chem. Phys.* **2024**, *160*, 154112. <https://doi.org/10.1063/5.0204986>
- [33] C. Schran, J. Behler, D. Marx, *J. Chem. Theory Comput.* **2020**, *16*, 88–99. <https://doi.org/10.1021/acs.jctc.9b00805>
- [34] H.-G. Yu, H. Song, M. Yang, *J. Chem. Phys.* **2017**, *146*, 224307.
- [35] O. Vendrell, F. Gatti, H.-D. Meyer, *J. Chem. Phys.* **2009**, *131*, 034308.
- [36] L. D. Landau, E. M. Lifshitz, *Quantum Mechanics: NonRelativistic Theory*, Pergamon Press, Oxford, 2nd edn., **1965**.
- [37] C. Herring, *Rev. Mod. Phys.* **1962**, *34*, 631–645. <https://doi.org/10.1103/RevModPhys.34.631>
- [38] M. T. Cvitaš and S. C. Althorpe, *J. Chem. Theory Comput.* **2016**, *12*, 787–803. <https://doi.org/10.1021/acs.jctc.5b01073>
- [39] M. T. Cvitaš, *J. Chem. Theory Comput.* **2018**, *14*, 1487–1500. <https://doi.org/10.1021/acs.jctc.7b00881>
- [40] P. R. Bunker, P. Jensen, *Molecular Symmetry and Spectroscopy*, NRC Research Press, Ottawa, 2nd edn., 2006.
- [41] D.-J. Liu, N. N. Haese, T. Oka, *J. Chem. Phys.* **1985**, *82*, 5368–5372. <https://doi.org/10.1063/1.448620>
- [42] D.-J. Liu, T. Oka, *Phys. Rev. Lett.* **1985**, *54*, 1787–1789. <https://doi.org/10.1103/PhysRevLett.54.1787>
- [43] M. Gruebele, M. Polak, R. J. Saykally, *J. Chem. Phys.* **1987**, *87*, 3347–3351. <https://doi.org/10.1063/1.453029>
- [44] J. Tang, T. Oka, *J. Mol. Spectrosc.* **1999**, *196*, 120–130. <https://doi.org/10.1006/jmsp.1999.7844>
- [45] M. H. Begemann, C. S. Gudeman, J. Pfaff, R. J. Saykally, *Phys. Rev. Lett.* **1983**, *51*, 554–557. <https://doi.org/10.1103/PhysRevLett.51.554>
- [46] M. H. Begemann, R. J. Saykally, *J. Chem. Phys.* **1985**, *82*, 3570–3579. <https://doi.org/10.1063/1.448914>
- [47] T. J. Sears, P. R. Bunker, P. B. Davies, S. A. Johnson, V. Špirko, *J. Chem. Phys.* **1985**, *83*, 2676–2685. <https://doi.org/10.1063/1.449270>
- [48] H. Petek, D. J. Nesbitt, J. C. Owruksy, C. S. Gudeman, X. Yang, D. O. Harris, C. B. Moore, R. J. Saykally, *J. Chem. Phys.* **1990**, *92*, 3257–3260. <https://doi.org/10.1063/1.457884>
- [49] D. J. Wales, *J. Chem. Phys.* **1999**, *110*, 10403–10409. <https://doi.org/10.1063/1.478972>
- [50] C. L. Vaillant, D. J. Wales, S. C. Althorpe, *J. Phys. Chem. Lett.* **2019**, *10*, 7300–7304. <https://doi.org/10.1021/acs.jpclett.9b02951>
- [51] Y.-C. Zhu, S. Yang, J.-X. Zeng, W. Fang, L. Jiang, D. H. Zhang, X.-Z. Li, *J. Am. Chem. Soc.* **2022**, *144*, 21356–21362. <https://doi.org/10.1021/jacs.2c09909>
- [52] K. Liu, J. G. Loeser, M. J. Elrod, B. C. Host, J. A. Rzepiela, N. Pugliano, R. J. Saykally, *J. Am. Chem. Soc.* **1994**, *116*, 3507–3512. <https://doi.org/10.1021/ja00087a042>
- [53] J. E. Lawrence, J. Dušek, J. O. Richardson, *J. Chem. Phys.* **2023**, *159*, 014111. <https://doi.org/10.1063/5.0155579>
- [54] E. Pollak, J. Cao, *J. Chem. Phys.* **2022**, *157*, 074109. <https://doi.org/10.1063/5.0106649>